JOURNAL OF QUATERNARY SCIENCE (2020) 1–10 ISSN 0267-8179. DOI: 10.1002/jqs.3195

JQS Journal of Quaternary Science QRA Quaternary Research Association

# Beach ridges of Dali Lake in Inner Mongolia reveal precipitation variation during the Holocene

MENGYAO JIANG,[1] ZHIYONG HAN,[1]* XUSHENG LI,[1]* YONG WANG,[2] THOMAS STEVENS,[3] JUN CHENG,[4] CUNJUAN LV,[1] YUWEN ZHOU,[1] QIANQIAN YANG,[1] ZHIWEI XU,[1] SHUANGWEN YI[1] and HUAYU LU[1]

[1]School of Geography and Ocean Science, Nanjing University, Nanjing 210093, China
[2]Geological Institute, Chinese Academy of Geological Sciences, Beijing 100037, China
[3]Department of Earth Sciences, Uppsala University, Villavägen 16, Uppsala, 75236, Sweden
[4]Key Laboratory of Meteorological Disaster, Nanjing University of Information Science and Technology, Nanjing, 210044, China

Received 12 November 2019; Revised 16 February 2020; Accepted 20 February 2020

ABSTRACT: Variability in East Asian summer monsoon precipitation during the Holocene remains of debate. In this study, we use a closed lake with well-dated lake beach ridges located on the margin of the East Asian summer monsoon, a region highly sensitive to monsoon precipitation changes, to obtain a temporal sequence of water volume in North China. The elevation of each beach ridge calibrated to the modern lake level was surveyed. Optically stimulated luminescence dating of undisturbed sediments of beach ridges was performed. The lake area and water volume corresponding to each beach ridge were calculated using a digital elevation model. This study reveals relatively reduced monsoon precipitation from ~12 to 7 ka interrupted by strengthening of the monsoon circulation to a maximum from ~7 to ~5 ka and followed by greatly reduced monsoon intensity until the present day. These results demonstrate that changes in the East Asian summer monsoon precipitation may not be directly driven by global temperature or atmospheric $CO_2$ content. Rather, we suggest that variation in the the monsoon margin precipitation is probably mainly driven by ice volume and subordinately by the summer solar insolation difference between mid-latitude land and low-latitude ocean. Copyright © 2020 John Wiley & Sons, Ltd.

KEYWORDS: beach ridge; Dali Lake; Holocene; lake water volume; optically stimulated luminescence (OSL)

## Introduction

The evolution of the East Asian summer monsoon (EASM) during the Holocene is vigorously debated. Despite extensive analysis, variability in the Holocene EASM is inconsistent not only between palaeoclimate records and climate models but also among different paleoclimate records (Chen *et al.*, 2016; Goldsmith *et al.*, 2017; Liu *et al.*, 2017). Cave speleothem $\delta^{18}O$ records in regions affected by the EASM indicate the strongest EASM during the early Holocene (Dykoski *et al.*, 2005; Wang *et al.*, 2008; Dong *et al.*, 2010). This interpretation is termed the wet early Holocene herein and is supported by a reconstructed monsoon precipitation record from lacustrine sediments in Dali Lake, which is situated in the marginal monsoon area of North China (Goldsmith *et al.*, 2017). In comparison to the wet early Holocene, the wet middle Holocene represents a different scenario, with the strongest EASM during the middle Holocene (Lu *et al.*, 2005, 2013b; Xu *et al.*, 2010; Chen *et al.*, 2015; Wen *et al.*, 2017; Zhou *et al.*, 2018). A geographically variable monsoon (An *et al.*, 2000) or westerly-dominated climate (Chen *et al.*, 2006) cannot explain the monsoon discrepancy because these records are recovered from closely adjacent sites located in the same climate zone affected by the monsoon today.

The precipitation in monsoon marginal regions is very sensitive to climate change (Lu *et al.*, 2005) and is mainly determined by migration of the EASM (Zhou *et al.*, 2018). Located in the monsoon marginal region in northern China, Dali Lake is in the transition belt between an EASM-dominated climate and a continental climate, which is an ideal region for reconstructing the changes in monsoon precipitation. However, the reconstructed lake level records remain controversial. The lake level fluctuation was inferred from geochemical, mineralogical, sedimentological and palaeontological data from an accelerator mass spectrometry $^{14}C$-dated sediment core recovered from the depocentre of Dali Lake. Different timings of the highstands have been determined: 11.5–7.6 ka (Xiao *et al.*, 2008), 9.8–7.1 ka (Xiao *et al.*, 2009), 7.7–5.9 ka (Fan *et al.*, 2017, 2019) and 8.3–6.0 ka (Wen *et al.*, 2017). Another study on lake sediments, alluvial deposits and four beach ridges yielded four periods of highstand, i.e. 11.5–11, 10.5–9.5, 8.3–7.8 and 6.1–5.9 ka (Goldsmith *et al.*, 2017).

In contrast to many proxies, such as geochemical and biological indicators, the variation in water volume in a closed lake fed by rainfall can be directly interpreted as precipitation-driven, as discussed below (Smith and Street-Perrott, 1983; Reheis *et al.*, 2014). Furthermore, among the evidence used to reconstruct past lake levels, beach ridges are preferred because they are direct indicators of the positions of the ancient shoreline. A closed lake with multilevel beach ridges can be regarded as a natural hyetometer, providing accurate proxy data for relative changes in precipitation.

In this study, we investigated the geomorphological and sedimentary characteristics of the beach ridges of Dali Lake. A topographical survey and numerical dating were carried out to reconstruct the palaeo-hydrological parameters. Monsoon precipitation change is interpreted based on the temporal sequence of the lake water volume.

## Study region

### *Geographical setting*

Dali Lake (43°15′N, 116°30′E), a barrier lake dammed by volcanic lava during the Pleistocene (Gao, 1988), is situated in the northern Hunshandake sandy land in North China

*Correspondence: Z. Han, and X. Li, as above.
E-mail: zyhan@nju.edu.cn; lixusheng@nju.edu.cn

(Fig. 1a,b). The lake is 227 km$^2$ in area, with a drainage area of 4515 km$^2$, a modern lake level of ~1226 m above sea level (a.s.l.) (Xiao *et al.*, 2008) and a water volume of 2.0 km$^3$. Maximum water depth is 11 m (Xiao *et al.*, 2008), with shallower waters in the east and deeper waters in the west. Lake cliffs are developed at the margin of a basalt platform around Dali Lake, and these show that the highest lake level reached an elevation of ~1295 m as indicated by a wave-cut platform (Fig. 1c).

To the south, Dali Lake is surrounded by the Hunshandake sandy land. The basalt platform delimitates the lake in the north and west. The Gongger grassland neighbouring the Great Hinggan Range is situated to the east of Dali Lake. The Gongger River that originates from the Great Hinggan Range feeds the lake and supplies 75% of the total water inflow (Compilatory Commission of Annals of Hexigten Banner, 1993). The modern natural vegetation of the Dali Lake basin is categorized as a middle temperate steppe.

The catchment of Dali Lake is influenced by the margin of the EASM precipitation and is dominated by a climate with a long cold winter and a large temperature difference between day and night. According to the records of meteorological stations at Xilinhaote (55 km to the north-west), from 1957 to 2001, annual temperature ranged from −0.2 to 4.4 °C with an average of 3.2 °C, annual precipitation ranged from 121 to 561 mm with an average of 280 mm, and annual pan evaporation varied from 1521 to 2270 mm with an average of 1828 mm. Annual pan evaporation was more than 6.5 times the annual rainfall. The average frost-free period was 100–110 days. Average July and January temperatures were 22 and −19 °C, respectively. Nearly 90% of the annual precipitation and 83% of the annual pan evaporation occurred in the summer half-year (from April to September) (Fig. 2).

## Characteristics of beach ridges

Lake cliffs, representing the highest lake level once reached, developed on the basalt platform around the lake basin. The now-dry lake bed between the lake cliff and the modern shoreline is up to ~12 km wide in the northern lake basin, where multilevel beach ridges are preserved. We found 13 beach ridges of different elevations ranging from 1233.3 to 1282.3 m in this area (Fig. 1c,d), which indicate the positions of past lake waterlines. Generally, the upper part of the dry lake bed, where 12 beach ridges have developed, is steeper than the lower part (Fig. 3). Clearly, the steep lake bed may facilitate the development of beach ridges.

These beach ridges have distinct features that aid identification, including a ridge-like landform distributed along the contour line, clastic sediments composed of gravels and sands, and a coarsening-upward sequence. The observed beach ridges generally have a broad and gentle shape and a symmetrical form ~15 m wide and ~0.8 m high. They can extend up to several kilometres in length at the same elevation (Supporting Information Fig. S1a,c).

The sedimentary facies are exposed by trenching on the crest of each beach ridge. All beach ridges exhibit a similar sedimentary sequence, including an upper and a lower horizon (Fig. 3). The upper horizon of a ridge is composed of poorly sorted gravelly mud or gravelly muddy sand ~20 cm thick, which represents the final phase of lacustrine deposition or post-depositional reworking. The lower horizon of a ridge is

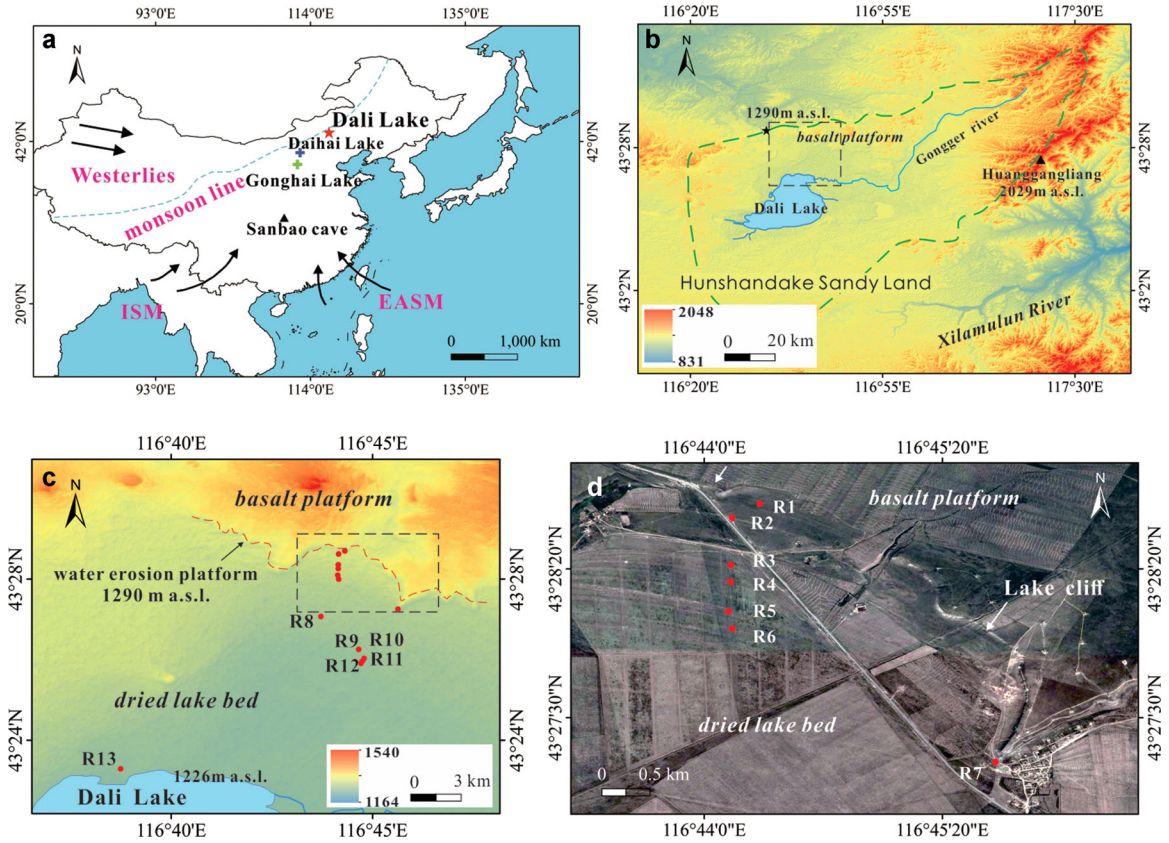


**Figure 1.** Location of Dali Lake and the terrain of the drainage basin. (a) Main climatic systems of East Asia including the East Asian summer monsoon (EASM), Indian summer monsoon (ISM) and westerlies. The green dashed line shows the modern summer monsoon boundary. Relevant sites include Dali Lake (red star), Daihai Lake (blue cross), Gonghai Lake (green cross) and Sanbao Cave (black triangle). (b) Drainage basin (dashed cyan line) of Dali Lake on a DEM map (data from www.91weitu.com). The black star indicates the potential spillway. (c) DEM map generated using ArcGIS 10.1 (www.esri.com/software/arcgis). (d) Satellite image (data from Google Earth) showing that beach ridges are well developed below the lake cliff (marked by white arrows). [Color figure can be viewed at wileyonlinelibrary.com]

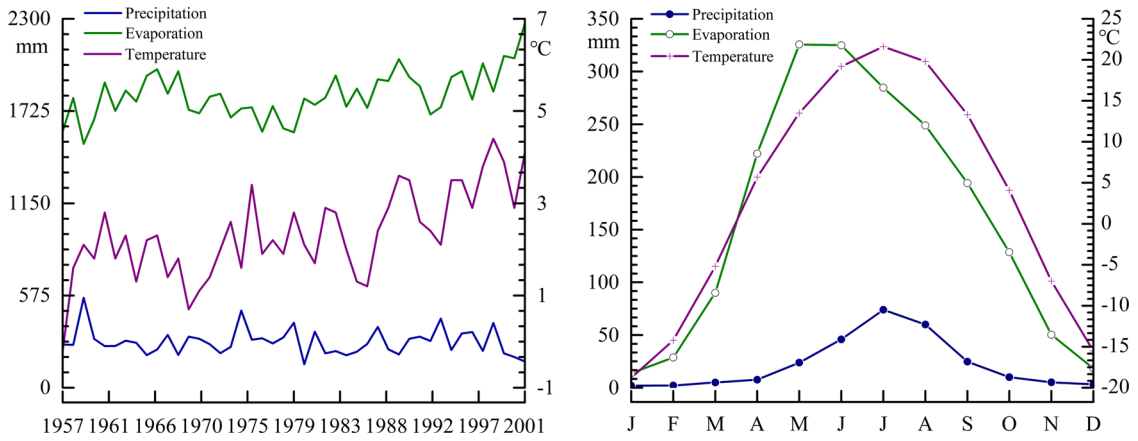


**Figure 2.** Annual (left) and monthly (right) temperature, precipitation and pan evaporation for the period 1957–2001 at a meteorological station at Xilinhaote (data from data.cma.cn). [Color figure can be viewed at wileyonlinelibrary.com]

composed of moderately sorted gravelly sand or sandy gravel, sometimes containing fragments of mollusc shells. Parallel bedding can be seen within beach ridges (Fig. S1b). The gravel texture is similar to that of the modern beach, with clasts that are rounded and smaller than ~ 5 cm. The beach ridges are labelled R1–R13 from highest to lowest elevation.

## Materials and methods

### *Topographic survey*

The elevation of each beach ridge was surveyed using a DS3 level instrument calibrated to the modern lake level (43.37°N, 116.63°E), which is 1226 m a.s.l. The topography of the lake basin was derived through a 1: 25 000 digital elevation model (DEM) (data from www.91weitu.com) and lake bottom sounding (Xiao *et al.*, 2008). The lake area and water volume corresponding to each beach ridge were calculated using ArcGIS10.1. Errors of the lake area and water volume are given by accounting for the mean elevation error of ±2 m.

### *OSL techniques*

To avoid the influence of any post-depositional processes on numerical dating, samples were collected from the lower horizon for optically stimulated luminescence (OSL) dating. Stainless steel tubes 30 cm long were hammered into the sediments exposed in a trench. The tube full of sediment was sealed and brought to the OSL laboratory at Nanjing University.

The formation age of each beach ridge was determined by using the OSL dating method. An OSL age is calculated using an estimate of the total absorbed dose since the last exposure to sunlight, termed the equivalent dose ($D_e$), and the dose rate of ionizing radiation (Aitken, 1998). Quartz grains with diameters of 90–125 or 125–250 μm were extracted using standard procedures, including treatment with 10% hydrochloric acid and 30% hydrogen peroxide to remove carbonates and organic matter, respectively, followed by wet sieving. After this treatment, 40 min of 40% hydrofluoric acid etching and hydrochloric acid rinsing were conducted to obtain pure quartz grains. The purity of the quartz was determined using the OSL-infrared (IR) depletion ratio method (Jacobs *et al.*, 2003).

Except for sample DLH-R8, for which 46 aliquots were used, 16 aliquots were used to measure the $D_e$ values of all other samples using the single-aliquot regenerative-dose (SAR) procedure (Murray and Wintle, 2000, 2003) performed on a Risø TL/OSL-DA-20C/D reader fitted with blue–green diodes (470 ± 30 nm; 40 mW cm$^{-2}$) and an IR laser diode (830 nm).

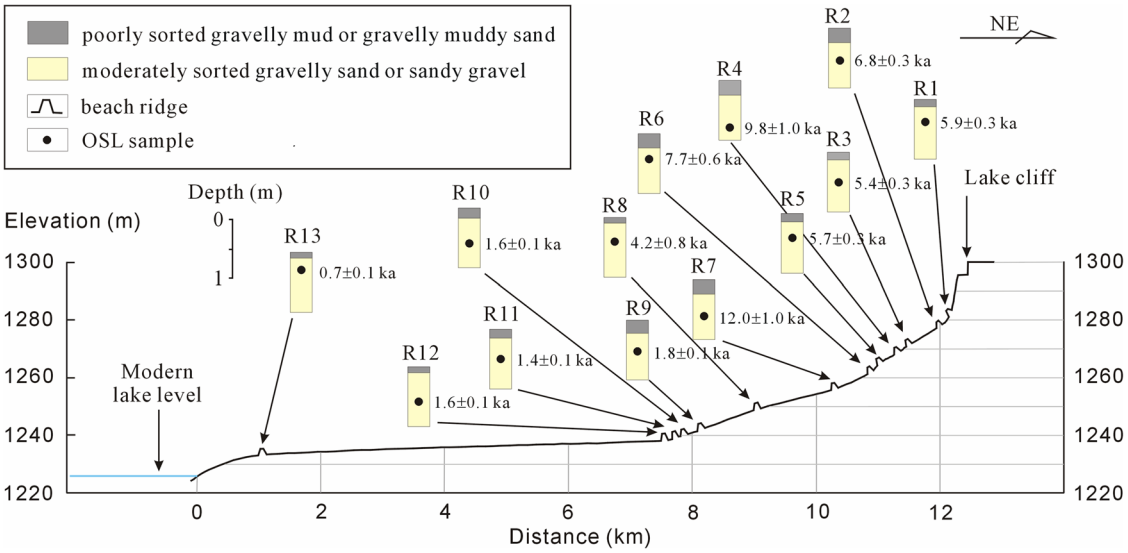


**Figure 3.** Schematic profile showing the landforms of the dry lake bed and the sites of the beach ridges to the north of Dali Lake. Stratigraphic columns and sampling positions for each beach ridge are also given. Numbers next to the stratigraphic column are OSL ages. [Color figure can be viewed at wileyonlinelibrary.com]

The luminescence signal was detected through 7.5-mm Hoya U-340 filters. Irradiation was carried out using a $^{90}Sr/^{90}Y$ beta source built into the reader. The signal was integrated for the first 0.32 s of stimulation time minus a background estimated from 0.32–0.64 s of stimulation. All growth curves were fitted using a single exponential function (Fig. 4a,b).

Preheat plateau tests and dose recovery tests were conducted on samples DLH-R4 and DLH-R8. According to the preheat plateau test, a 240 °C preheat and a 200 °C cutheat were selected for the SAR $D_e$ determination procedure (Fig. 4c). The dose recovery test is now widely used to check the reliability of a measurement procedure (Murray and Wintle, 2003). The ratios of the recovered dose to the given dose (which is close to the natural $D_e$) are 0.98 and 0.94, respectively. The $D_e$ values are given as the weighted arithmetic means of each set of aliquots and are presented along with the standard errors.

Figure 4(d) illustrates the $D_e$ distributions of representative sample DLH-R8 from the Abanico Plot (Dietze *et al.*, 2016). Most aliquots are clustered around the ± 2 SD band region, which is centred at the mean, and the OD value is 25%. Overdispersion has also been observed for well-bleached aeolian sediments (Lian and Roberts, 2006; Lee *et al.*, 2009); thus, the samples' grains probably experienced sufficient sunlight exposure before deposition.

Dose rates were calculated from uranium, thorium and potassium contents measured using neutron activation analysis (NAA). We calculated the dose rate via DRc, a free Java application (Tsakalos *et al.*, 2016). The OSL age is given by $D_e$ divided by the dose rate.

## Results

### *Reconstructed lake parameters*

The elevations of the measured beach ridges range from 1233.3 to 1282.3 m, giving a 49-m elevation difference between the highest (R1) and the lowest (R13) beach ridges (Table 1). The elevation difference between neighbouring beach ridges ranges from 0.7 to 7.2 m with an average of 4.1 m. Correspondingly, a 3.6-fold change in lake area and a 10.9-fold change in water volume were observed, ranging from 1320.5 ± 55.6 to 366.4 ± 34.4 $km^2$ and from 43.4 ± 3.3 to 4.0 ± 0.8 $km^3$, respectively (Table 1). The error in the lake area introduced from the uncertainty in the DEM varies from 3.2 to 10.6% with an average of 6.0%. The error in the water volume introduced from the uncertainty in the DEM varies from 7.3 to 25.8% with an average of 12.9%. The error is small compared with the amplitude of the lake fluctuations, and the reconstructed lake parameters indicate meaningful lake fluctuation in the past.

### *OSL ages*

OSL ages are dependent on the water content of the sample. In addition to the water content measured for the natural samples (i.e. the measured water content), we also measured the saturated water content, the average value for 13 samples being 20%. Generally, the elevations of beach ridges younger than R1 (5.9 ± 0.3 ka) increase with OSL age, while those of ridges older than R1 decrease with age (Table 2). This allows us to estimate the influence of water content on the OSL age.

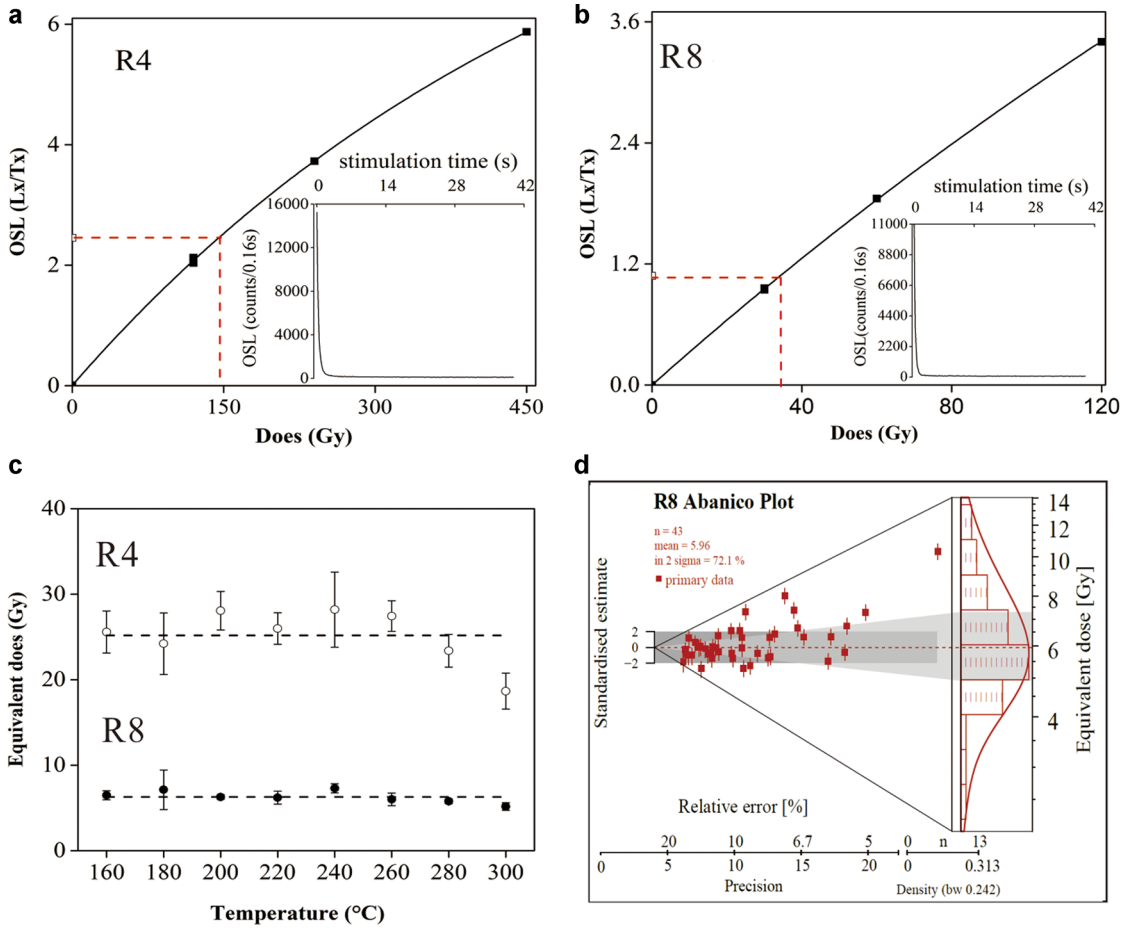


**Figure 4.** Coarse-grain quartz luminescence characteristics. (a,b) Typical dose–response curves for aliquots of samples R4 and R8, respectively (inset shows the natural decay curves). The red dashed line indicates the natural OSL signal and the resulting $D_e$ values. (c) Preheat plateau tests of samples R4 and R8. Three aliquots were measured at each temperature, and error bars represent two standard errors. The dashed line is drawn at the average $D_e$ over the 180–300 °C interval. (d) Abanico plot of $D_e$ determination for sample R8. [Color figure can be viewed at wileyonlinelibrary.com]

**Table 1.** Elevations of beach ridges and corresponding lake areas and water volumes.

| Beach ridge | Elevation (m) | Water area ($km^2$) | Water volume ($km^3$) |
|---|---|---|---|
| R1 | 1282.3 | 1320.5 ± 55.6 | 43.4 ± 3.3 |
| R2 | 1277.8 | 1214.4 ± 46.3 | 38.4 ± 2.8 |
| R3 | 1271.4 | 1059.7 ± 36.2 | 30.5 ± 2.4 |
| R4 | 1268.6 | 1025.7 ± 32.5 | 28.5 ± 2.2 |
| R5 | 1265.1 | 961.3 ± 34.9 | 24.5 ± 2.1 |
| R6 | 1262.0 | 904.6 ± 38.6 | 21.7 ± 2.0 |
| R7 | 1256.2 | 787.5 ± 43.3 | 16.7 ± 1.8 |
| R8 | 1249.0 | 636.7 ± 37.3 | 11.8 ± 1.4 |
| R9 | 1242.1 | 515.8 ± 41.4 | 7.8 ± 1.2 |
| R10 | 1240.1 | 465.1 ± 40.2 | 6.9 ± 1.1 |
| R11 | 1239.4 | 449.9 ± 29.6 | 6.4 ± 1.0 |
| R12 | 1238.2 | 434.9 ± 28.1 | 6.0 ± 0.9 |
| R13 | 1233.3 | 366.4 ± 34.4 | 4.0 ± 0.8 |
| Modern Lake | 1226.0 | 232.8 ± 24.7 | 2.0 ± 0.5 |

The old beach ridges (>5.9 ± 0.3 ka) were inundated and did not emerge from the water until the lake level dropped below their elevation after 5.9 ± 0.3 ka. We can assume that the sediments were saturated with water before their emergence and have maintained their water content around the measured value since emerging. Thus, the OSL age of a once-submerged beach ridge is calculated by iteration of time-weighting of dose rates based on the measured and saturated water contents (Table 2). The ages of the submerged beach ridges increase when the saturated water content is considered, and we use these age data for analysis (Table 2). This result also demonstrates that the uncertainty in the water content due to unknown lake level fluctuations has a slight influence on the OSL age. The calibrated OSL ages show that the beach ridges were deposited between 12.0 ± 1.0 and 0.7 ± 0.1 ka.

### *Lake water fluctuations*

The resulting temporal sequence of lake water parameters reconstructed from Dali Lake shows variability during the Holocene, for example a medium lake volume between c. 12 and 7 ka, increasing to a maximum between 7 and 5 ka and then decreasing abruptly before trending towards the current lowstand (Fig. 5). The lake level reached 1268.6 m a.s.l. (lake area of 1025.7 $km^2$; water volume of 28.5 $km^3$) c. 9.8 ka and further rose to a maximum of 1282.3 m a.s.l. (lake area and water volume increased to 1320.5 $km^2$ and 43.4 $km^3$, respectively) c. 5.9 ka. Lake volume at c. 9.8 ka was approximately 14 times greater than at present and was nearly 21 times the present volume at c. 5.9 ka. A dramatic decrease to 24.5 $km^3$ took place at c. 5.7 ka. This change was followed by a slower general decrease after 4.2 ka, where the water volume decreased from 11.8 to 4.0 $km^3$ by 0.7 ka and continuously decreased to the present 2.0 $km^3$. As such, the water volume of Dali Lake was relatively high during the early Holocene (12.0–7.7 ka), peaked during the middle Holocene (6.8–5.4 ka) and then continuously decreased to a Holocene minimum during the late Holocene (after 4.2 ka).

## Discussion

### *Preservation of submerged beach ridges*

Four beach ridges, namely R2, R4, R6 and R7, are older than the highest (R1), which indicates that these four beach ridges were once inundated when the lake level reached R1 and emerged when the lake level dropped again. Survival of a beach ridge in this scenario is due to the specific sedimentary

**Table 2.** Results of OSL dating of Dali Lake beach ridges. Ages are calculated for different water contents, including the measured water content and saturated water content. Ages are also calibrated for inundated beach ridges assuming a saturated water content during inundation.

| Field no. | Depth (m) | Aliquot | Grain size (μm) | Saturated water content (%) | Measured water content (%) | U (p.p.m.) | Th (p.p.m.) | K (%) | Dose rate (Gy $ka^{-1}$) | $D_e$ (Gy) | Age for measured water content (ka) | Age calibrated for inundation (ka) |
|---|---|---|---|---|---|---|---|---|---|---|---|---|
| R1 | 0.4 | 16 | 125–250 | 18.7 | 2.1 | 0.62 ± 0.05 | 2.05 ± 0.10 | 1.44 ± 0.05 | 2.00 ± 0.10 | 11.7 ± 0.2 | 5.9 ± 0.3 | |
| R2 | 0.5 | 16 | 125–250 | 10.3 | 1.4 | 0.81 ± 0.05 | 3.92 ± 0.15 | 1.43 ± 0.05 | 2.17 ± 0.10 | 14.5 ± 0.2 | 6.7 ± 0.3 | 6.8 ± 0.3 |
| R3 | 0.5 | 16 | 63–90 | 24.6 | 4.4 | 0.92 ± 0.05 | 3.88 ± 0.14 | 1.98 ± 0.06 | 2.74 ± 0.07 | 14.9 ± 0.7 | 5.4 ± 0.3 | |
| R4 | 0.8 | 16 | 90–125 | 32.5 | 7.9 | 1.21 ± 0.06 | 4.89 ± 0.17 | 1.85 ± 0.06 | 2.50 ± 0.09 | 22.3 ± 1.3 | 8.9 ± 0.6 | 9.8 ± 1.0 |
| R5 | 0.4 | 16 | 125–250 | 14.2 | 0.9 | 0.98 ± 0.05 | 4.45 ± 0.16 | 1.67 ± 0.06 | 2.49 ± 0.12 | 14.2 ± 0.4 | 5.7 ± 0.3 | |
| R6 | 0.4 | 16 | 90–125 | 16.1 | 1.1 | 0.72 ± 0.05 | 2.66 ± 0.12 | 1.27 ± 0.05 | 1.97 ± 0.09 | 14.2 ± 0.9 | 7.2 ± 0.6 | 7.7 ± 0.6 |
| R7 | 0.6 | 16 | 125–250 | 16.2 | 0.9 | 0.52 ± 0.04 | 2.01 ± 0.08 | 0.44 ± 0.03 | 1.03 ± 0.03 | 10.9 ± 0.4 | 10.6 ± 0.5 | 12.0 ± 1.0 |
| R8 | 0.4 | 46 | 125–250 | 21.3 | 0.5 | 0.51 ± 0.04 | 2.17 ± 0.10 | 0.91 ± 0.04 | 1.49 ± 0.04 | 6.3 ± 1.1 | 4.2 ± 0.8 | |
| R9 | 0.5 | 16 | 125–250 | 22.5 | 0.8 | 0.73 ± 0.05 | 3.54 ± 0.14 | 1.40 ± 0.05 | 2.11 ± 0.10 | 3.8 ± 0.2 | 1.8 ± 0.1 | |
| R10 | 0.6 | 16 | 125–250 | 15.4 | 3.1 | 0.97 ± 0.05 | 3.36 ± 0.13 | 1.16 ± 0.04 | 1.87 ± 0.09 | 3.0 ± 0.2 | 1.6 ± 0.1 | |
| R11 | 0.5 | 16 | 125–250 | 17.0 | 4.0 | 0.76 ± 0.05 | 3.33 ± 0.13 | 1.38 ± 0.05 | 2.01 ± 0.10 | 2.8 ± 0.1 | 1.4 ± 0.1 | |
| R12 | 0.6 | 16 | 90–125 | 30.0 | 6.2 | 1.40 ± 0.07 | 5.20 ± 0.18 | 2.40 ± 0.07 | 3.24 ± 0.10 | 5.2 ± 0.4 | 1.6 ± 0.1 | |
| R13 | 0.35 | 16 | 125–250 | 23.7 | 0.3 | 0.62 ± 0.05 | 2.32 ± 0.10 | 1.65 ± 0.05 | 2.26 ± 0.11 | 1.5 ± 0.1 | 0.7 ± 0.1 | |

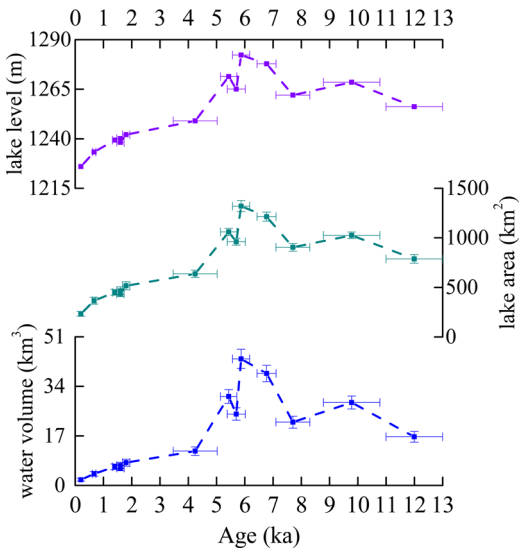


**Figure 5.** Reconstructed variability of Dali Lake water during the Holocene. [Color figure can be viewed at wileyonlinelibrary.com]

process. Compared to other lakeshore sediments, beach ridges are deposited on only high-energy beaches (i.e. wave-dominated lakeshores). The wave propagates landward and transforms gradually in shallow water. The shallower the water, the coarser the sediments that the wave can transport (Supporting Information, Fig. S2a). As a result, the sediments become coarser towards the shoreline. Of course, the winnowing of fine-grained materials can also result in the coarsening of sediments. The coarsest sediments, which are usually coarse sands and gravel, are transported by the swash and accumulate there. One beach ridge (BR2) appeared when the coarsest sediments aggraded (Fig. S2a).

With lake level rise, the beach ridge (BR2) will be inundated. Another beach ridge (BR1) will then develop at a higher position (Fig. S2b). The submerged beach ridge (BR2) cannot be altered to any great extent because the wave energy is lower than the swash. Instead of erosion, aggradation of fine sediments, usually sand and silt on the submerged beach ridge (BR2), will take place (Fig. S2b). When the lake level drops, the submerged beach ridge (BR2) will again be affected by the stronger waves. Aggraded fine sediments may be easily eroded. However, the coarse beach ridge sediments of BR2 will remain *in situ* unless the recurring wave is stronger than the wave that occurred when BR2 formed (Fig. S2c). Of course, the duration of the recurring wave acting on BR2 should be long enough to completely destroy BR2. Therefore, whether a submerged beach ridge will survive depends mainly on the recurring wave energy and the duration that the water level remains at the position of the submerged beach ridge. When the lake drops further, a young beach ridge (BR3) may be deposited at the lower position. The sediments beneath BR3 are relatively fine because they are deposited in deeper water (weak wave energy) (Fig. S2d).

Previous studies have reported that beach ridges occur on both lakeshores and seashores, such as at St Lucia lake in South Africa (Botha *et al.*, 2018), Tangra Yum Co in Tibet (Rades *et al.*, 2015) and the coastal zone in north-eastern Australia (Nott *et al.*, 2009). Two studies on Dali Lake have demonstrated the existence of surviving beach ridges (Liu *et al.*, 2016; Goldsmith *et al.*, 2017). Our study reproduces this phenomenon with more beach ridges.

Therefore, beach ridges can only record part of the fluctuation in water level. Some water levels have left no beach ridges, and some submerged beach ridges have been destroyed. Thus, our reconstructed lake level can only reflect the main fluctuations during the Holocene.

## *Precipitation dominated lake water fluctuations*

Variations in lake volume respond to the balance between lake inflow and output. Evaporation from the lake surface is the only output for a closed lake in a semi-arid area, such as Dali Lake, because ground water loss out of the lake is very small and can be neglected (Goldsmith *et al.*, 2017). Thus, the steady-state water balance equation of a closed lake can be expressed as $P \times A1 + \alpha \times P \times A2 = E \times A1$, where P is annual precipitation, E is annual lake evaporation, α is the runoff coefficient, A1 is the lake area and A2 is the drainage basin area. If we assume that Holocene annual precipitation was constant and equal to 400 mm and that the modern annual lake evaporation is 900 mm, α is thus approximately 0.06 for a 232-km$^2$ lake area and 4515-km$^2$ drainage basin area. Assuming the same α value, this would result in a lake volume increase to ~4 km$^3$ under a 687 mm a$^{-1}$ evaporation regime and to ~16.7 km$^3$ under a 521 mm a$^{-1}$ evaporation regime. Therefore, unrealistically low evaporative regimes would be required to achieve the lake level increases seen in our record, given that the current pan evaporation is 1828 mm. Thus, changes in evapotranspiration cannot be the main cause of the immense fluctuations in water volume in Dali Lake.

Other potential drivers of lake level can also be excluded. Fluctuations in the water table can affect lake levels (Almendinger, 1990). Indeed, a dramatic drop of 30 m in the water table in the Hunshandake sandy land due to headward erosion of the Xilamulun River at 4.2 ka has previously been suggested (Yang *et al.*, 2015). However, the riverbed reached its present elevation by 7.9 ka, and no evident river incision has been found since then (Lv *et al.*, 2018). The proposed drop in the water table is still smaller than the 56 m lowering of the lake level seen from the beach ridges here. Although both Dali Lake and the Xilamulun River are situated in the same sandy land, they are separated by a distance of 35 km, and a watershed with an elevation of 1320–1450 m lies between them. This topographic setting greatly reduces the influence of the Xilamulun River on Dali Lake. In addition, a wave-cut platform is developed beneath the lake cliff at an elevation of ~1295 m (Fig. 1). This platform is approximately 10 m higher than the uppermost beach ridge, and this difference excludes the possibility of any overspill when the lake level reached only the position of the studied beach ridges. Furthermore, the influence of tectonic movement on water volume is considered to be negligible as no indications of neotectonics have been found in the area. Finally, to the south of Dali Lake, stable and semi-stable dunes are developed in the Hunshandake sandy land. The basal ages of most dunes are concentrated from 15 to 13 ka, and the main body is dated to the Holocene (Zhou *et al.*, 2013), which implies that these dunes have barely migrated during the Holocene. Immobile dunes demonstrate that no obvious topographical changes have occurred in the sandy land, which may alter the lake shore and further result in a change in water volume.

Based on the exclusion of all other potential drivers of water volume in Dali Lake, we propose that the main factor affecting the lake water volume is precipitation. Precipitation during the summer half-year accounts for up to 90% of the annual precipitation at present (Fig. 2), which indicates that water volume is a non-linear function of EASM precipitation. There is no evidence that winter precipitation can induce a substantial increase in annual precipitation in this region. If this climate pattern reflects the conditions of the past, the aforementioned relationship will exist for the Holocene. Thus, the greater the

lake volume, the higher the monsoon precipitation. Remote sensing and meteorological data confirm this finding and show that lake water volume increases with the strengthening of monsoon precipitation with no time delay (Han *et al.*, 2007; Zhang *et al.*, 2012). Therefore, the timing of the lake level highstands from the beach ridges above show that moderate monsoon precipitation occurred during the early Holocene (12.0–7.7 ka), followed by the most intense monsoon period during the middle Holocene (6.8–5.4 ka) and then a continuous and slow reduction in monsoon intensity after 4.1 ka during the late Holocene (Fig. 5). Thus, the precipitation record reconstructed from the beach ridges of Dali Lake supports a wet middle Holocene with EAM monsoon variation during the Holocene.

## *Comparison with other reconstructed lake fluctuations*

This study reveals the lake level fluctuations as well as lake area and water volume fluctuations of Dali Lake during the Holocene. Although lake level fluctuations have previously been determined using direct sedimentary evidence or inferred from proxy indicators, the latter two hydrological parameters have not been reported until now. A detailed study of the lake level fluctuations of Dali Lake was performed based on both beach ridges and other sediments (Goldsmith *et al.*, 2017). The reconstructed record shows that a highstand occurred between c. 13 and 5 ka and the early Holocene highstand was interrupted by two lowstands at c. 12 and c. 11 ka.

Some similarities are observed between Goldsmith's record and our own (Fig. 6). First, both records show that the highest stand occurred at c. 6 ka if the elevation difference between the lake level and the corresponding lake sediments is negligible. Second, both records show that lake level during the middle Holocene was higher than that during the early Holocene as a whole. Goldsmith *et al.* (2017) claimed that the lake reached highstands at 11–5.5 ka. In fact, the lake stood slightly higher at 8–6 ka than at 12–10 ka (Fig. 6b).

However, certain differences between the two records are noteworthy. For example, a declining tendency of the lake level after 4.2 ka is clearly confirmed by our record, which cannot be demonstrated by Goldsmith's record because there are no data for this period. Goldsmith's record indicates two highstands during the middle Holocene: one at 6.2 ka (1290 m) and another at 7.8 ka (1280 m). However, there is only one highstand at 5.9 ka (1282.3 m) in our record (Fig. 6c).

In addition, Goldsmith's record reveals that the lake level ranged from 1230 to 1279 m during the early Holocene and was unstable, probably underwent rising, declining and rising again (Fig. 6b). The data in our record display only a moderate variation ranging from 1256 to 1268 m. Our data for the early Holocene almost fall on the trend line if a polynomial trend line is added after removing alluvium samples, which are not relevant to the lake level (Fig. 6d). Hence, both our data alone or the combined dataset reveal a highstand during the middle Holocene. Our record has two obvious advantages over previous records. First, the lake fluctuation is well defined by additional beach ridges. Goldsmith *et al.* (2017) and Liu *et al.* (2016) studied only four and seven beach ridges, respectively. Second, the lake fluctuation is well defined by more reliable data. We only use OSL-dated beach ridges because only beach ridges can indicate the exact position of the lake level and OSL ages can explicitly represent the formation age of beach ridges. Radiocarbon-dated lake sediments were mainly used by Goldsmith *et al.* (2017) and Liu *et al.* (2016), which may result in uncertainties originating from the radiocarbon dating pertinent to the reservoir effect and re-deposition.

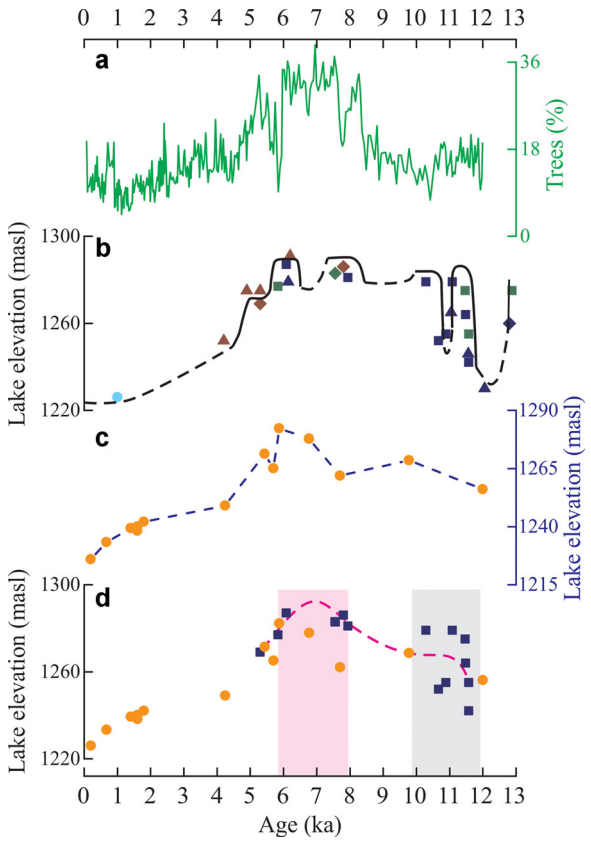


**Figure 6.** Comparison with other records from Dali Lake. (a) Pollen record (Wen *et al.*, 2017) of Dali Lake. The proportion of tree and shrub pollen is regarded as a reliable proxy for precipitation (Wen *et al.*, 2017). (b) Lake level record (Goldsmith *et al.*, 2017). (c) Lake level record (this study). (d) Combined data of this study (circles) and Goldsmith's study (squares) after removing alluvium samples. The dashed is the polynomial trend line for Goldsmith's data. The pink bar indicates the period of the lake highstand during the middle Holocene, and the grey bar indicates another period when the lake stood relatively low during the early Holocene. [Color figure can be viewed at wileyonlinelibrary.com]

Our record is generally similar to that given by a pollen study of a core in Dali Lake (Fig. 6a). The proportion of tree and shrub pollen acts as a reliable proxy for precipitation in northern China because increased precipitation will promote the expansion of forests. The percentages of tree and shrub pollen in core DL04 indicate that moderate precipitation occurred during the early Holocene, intensified precipitation occurred from c. 8.3 to c. 6 ka, and that there has been a gradually decreasing trend since then (Wen *et al.*, 2017). The general variations and some details are similar between the pollen-based record and our record. For example, the lowstands at 5.7 and 7.7 ka can be correlated to two periods of decreased precipitation, at 5.8 and 7.8 ka, respectively. Nevertheless, the pollen-based record indicates that low precipitation occurred during the early Holocene at levels comparable to that during the late Holocene.

## *Variations in the Holocene EAM*

TraCE-21ka is a state-of-art transient simulation of the global climate covering the period of the last 21 000 years using the fully coupled NCAR CCSM3 with a spatial resolution of T31 for the atmospheric and land components (3.75° × 3.75°, Collins *et al.*, 2006). According to palaeoclimate records, this simulation reasonably reproduced the climate transition from glacial to interglacial states (Shakun *et al.*, 2012; He *et al.*, 2013). TraCE-21ka yields both

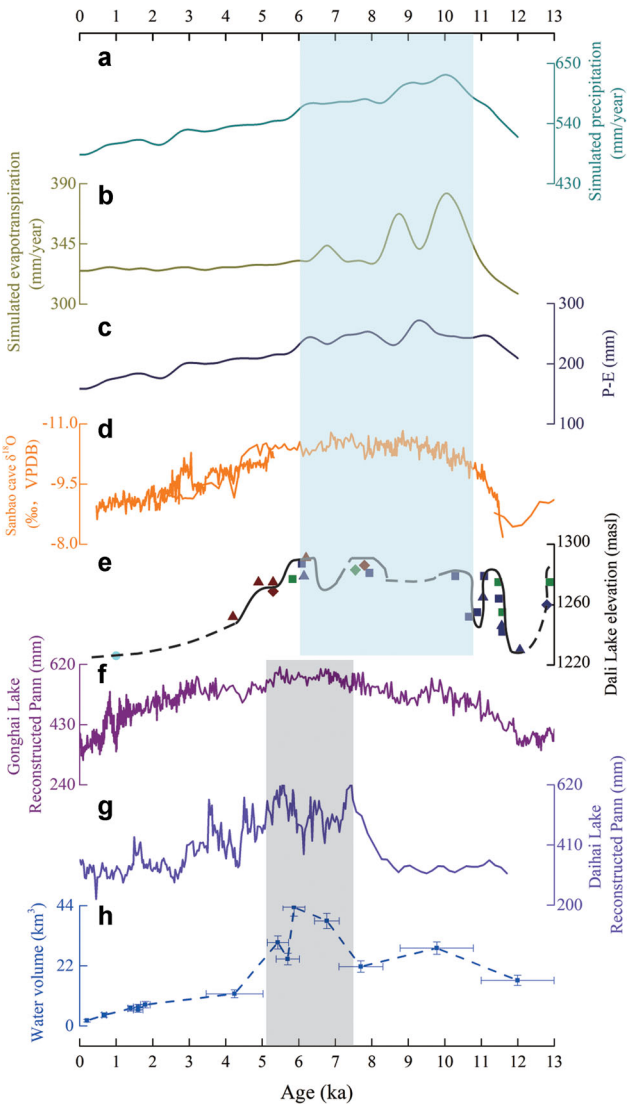


**Figure 7.** Water volume record of Dali Lake, a direct indicator of EASM precipitation, compared with other geological records and climate simulations. (a) CGCM-simulated annual precipitation since 12 ka (114.5–118.5°E, 41.25–45.25°N) (https://www.earthsystemgrid.org/project/trace.html). (b) CGCMsimulated annual evapotranspiration since 12 ka (114.5–118.5°E, 41.25–45.25°N) (https://www.earthsystemgrid.org/project/trace.html). (c) Simulated precipitation minus simulated evapotranspiration (P–E). (d) Sanbao cave speleothem $\delta^{18}O$ records (Wang *et al.*, 2008). (e) Lake level reconstructed for Dali Lake (Goldsmith *et al.*, 2017). (f) Pollen-based annual precipitation (Pann) reconstructed from Gonghai Lake (Chen *et al.*, 2015). (g) Pollen-based annual precipitation (Pann) reconstructed from Daihai Lake (Xu *et al.*, 2010). (g) Water volume record of Dali Lake since 12.0 ka with OSL ages; the lake volume errors are estimated by accounting for a mean elevation error of ±2 m (this study). The light blue bar indicates a wet early and middle Holocene and the grey bar a wet middle Holocene. [Color figure can be viewed at wileyonlinelibrary.com]

evapotranspiration (E) and precipitation (P) data for the grid area of the lake (114.5–118.5°E, 41.25–45.25°N) (https://www.earthsystemgrid.org/project/trace.html). The early Holocene is characterized by relatively high precipitation and evapotranspiration (Fig. 7a,b), and precipitation minus evapotranspiration (P – E) might represent a proxy indicator of the lake level; that is, a larger P – E corresponds to a higher lake level (Fig. 7c). If this assumption is true, then the TraCE-21ka results indicate a wet early and middle Holocene (from c. 11 to 6 ka). The inconsistency between the simulation and our results may be related to the difficulty in simulating regional monsoon patterns, especially along the monsoon margins, with a relatively coarse grid spacing.

In addition to Goldsmith's record (Fig. 7e), a wet early and middle Holocene is also observed in the speleothem oxygen isotope record in East Asia (Fig. 7d), which indicates that strong monsoons occurred at the same time (Wang *et al.*, 2008). Recent studies suggest that the lower speleothem $\delta^{18}O$ values indicate a stronger EASM circulation, which is characterized by enhanced monsoonal southerlies over East Asia (Liu *et al.*, 2014; Zhang *et al.*, 2018). Because the speleothem $\delta^{18}O$ values may reflect circulation changes independent of precipitation changes, the discrepancy between the $\delta^{18}O$ record and our precipitation record may be reconcilable.

The scenario of a wet early and middle Holocene is inconsistent with our reconstruction and other geological records (Xu *et al.*, 2010; Lu *et al.*, 2013b; Chen *et al.*, 2015; Zhou *et al.*, 2018). The most intense monsoon period during the middle Holocene can be inferred from other evidence. The effective humidity deduced from the proxy indicators in the sandy loess on the bank of Dali Lake shows that monsoon precipitation increased gradually during the early Holocene and reached its maximum at c. 6 ka. After 6 ka, precipitation decreased again (Zhou *et al.*, 2018).

Aeolian pollen data from lake sediments in adjacent regions are also approximately consistent with our findings that monsoon precipitation reached a maximum during the middle Holocene, although these records contain no clear sign of the remarkable decrease in precipitation shown in our data at ~5 ka (Fig. 7f,g) (Xu *et al.*, 2010; Chen *et al.*, 2015). Furthermore, some luminescence-dated sequences of loess on the Chinese Loess Plateau show a middle Holocene peak in magnetic susceptibility, which is a indicator of the summer monsoon (Lu *et al.*, 2013b). Thus, our precipitation record (Fig. 7h) is broadly consistent with several independent studies on a range of archives from the northern Chinese monsoon marginal areas.

Previous research suggests that global monsoon changes reflect multiple forcing factors, including solar radiation, ice

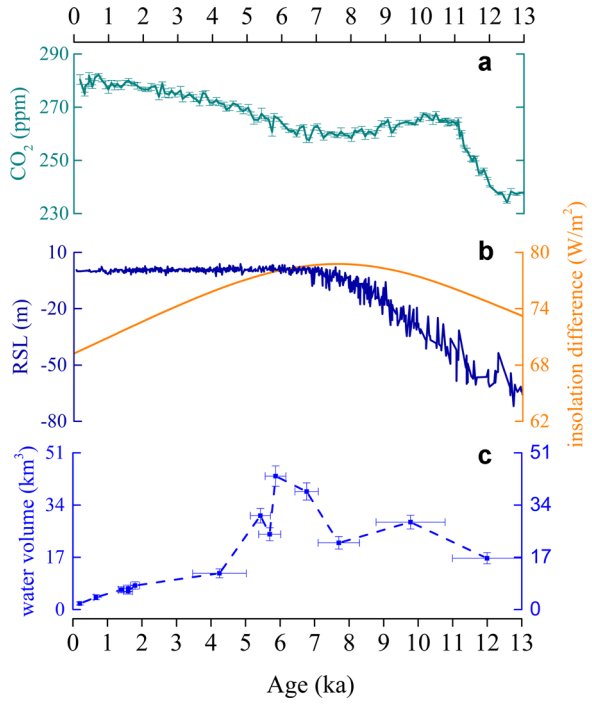


**Figure 8.** Comparison of the Dali Lake volume record with several factors potentially forcing monsoon climate change. (a) Reconstructed $CO_2$ record (Monnin *et al.*, 2004). (b) Relative sea level (RSL) record of the past 12 ka (Lambeck *et al.*, 2014) and 43°N summer (June to August) insolation (Laskar *et al.*, 2004). (c) Water volume record of Dali Lake since 12.0 ka with OSL ages. Lake volume errors are estimated by accounting for a mean elevation error of ±2 m (this study). [Color figure can be viewed at wileyonlinelibrary.com]

volume, melt water, greenhouse gases ($CO_2$, $CH_4$) and volcanic eruptions (An *et al.*, 2015). $CO_2$ has been suggested as an important factor in modulating the EASM since the Last Glacial Maximum (Lu *et al.*, 2013a), with higher Holocene $CO_2$ driving stronger monsoons. However, Holocene $CO_2$ changed inversely with monsoon precipitation in our record (Fig. 8), suggesting that at least on 1000-year timescales, $CO_2$ was not a notable factor in forcing the Holocene monsoon.

The index of land–sea thermal difference has been used to define the variation in the EASM circulation in summer (Sun *et al.*, 2002) (i.e. mid-latitude land and low-latitude sea in East Asia). Interestingly, we can see a close relationship between EASM intensity and summer solar insolation difference between 43°N and 5°N; generally, the larger the insolation difference, the stronger the EASM intensity (Fig. 8). The larger solar insolation difference may force the EASM to shift to regions at higher latitudes and enhance monsoon precipitation in monsoon marginal regions.

However, the insolation difference peak at ~7.8 ka pre-dates the ~6-ka EASM maximum. This time lag suggests that other factors also influence the EASM. Global ice volume has been proposed as a factor forcing changes in the EASM (Ding *et al.*, 2005). An experiment conducted with the IPSL_CM4 ocean–atmosphere coupled model show that the EASM is sensitive to the remnant ice sheet over North America and Europe, and the EASM at 9.5 ka (with remnant ice sheets present) was weaker than that at 6 ka (Marzin *et al.*, 2013). Monsoon precipitation increased approximately with decreasing ice volume until the mid-Holocene. The ice volume reached its minimum at c. 6 ka, which almost coincides with the timing of the EASM maximum (Fig. 8), implying that the ice volume plays a leading role in forcing the EAM changes. This primary forcing factor remained almost unchanged after the mid-Holocene, and thus the effects of the secondary factors on the EASM might become visible. This explains why we can see that the EASM weakens with the reduced summer insolation difference since the mid-Holocene (Fig. 8). This relationship may imply that the Holocene EASM is controlled by a combination of factors: first by global ice volume and second by solar radiation.

## Conclusions

Dali Lake in North China acts as a natural hyetometer because of its well-preserved abandoned beach ridges. The reconstructed lake water volume may reveal a wet middle Holocene in this region (i.e., the strongest EASM occurred during the middle Holocene). We suggest that the monsoon precipitation variation is probably driven mainly by ice volume and subordinately by the summer insolation difference between the mid- and low latitudes. This major discrepancy with traditional monsoon models suggests that our understanding of climate at the margin of the monsoon, or potentially the wider monsoon area in general, is inaccurate. Resolving this issue is crucial as the monsoon margin and its resident populations are especially sensitive to environmental changes.

## Supporting information

Additional supporting information may be found in the online version of this article at the publisher's web-site.

Supporting information.

*Acknowledgements.*. This work was supported by the National Natural Science Foundation of China (Nos. 41690111, 41671191, 41571188 and 41877451) and the China Geological Survey (No. DD20160120-07). The authors have no conflicts of interests to declare. The data are available at www.pangaea.de (https://doi.pangaea.de/10.1594/PANGAEA.905825).

*Abbreviations.* DEM, digital elevation model; DRc, dose rate calculator; EASM, East Asian Summer Monsoon; IR, infrared; ISM, Indian Summer Monsoon; NAA, neutron activation analysis; OSL, optically stimulated luminescence; RSL, relative sea level; SAR, single-aliquot regenerative-dose.

## References

Aitken MJ. 1998. *Introduction to Optical Dating: the Dating of Quaternary Sediments by the Use of Photon-Stimulated Luminescence*. Clarendon Press: Leeds.

Almendinger JE. 1990. Groundwater control of closed-basin lake levels under steady-state conditions. *Journal of Hydrology* **112**: 293–318.

An Z, Porter SC, Kutzbach JE. 2000. Asynchronous Holocene optimum of the East Asian monsoon. *Quaternary Science Reviews* **19**: 743–762.

An Z, Wu G, Li J. 2015. Global monsoon dynamics and climate change. *Annual Review of Earth and Planetary Sciences* **43**: 29–77.

Botha GA, Porat N, Haldorsen S *et al.* 2018. Beach ridge sets reflect the Late Holocene evolution of the St Lucia estuarine lake system. *South Africa. Geomorphology* **318**: 112–127.

Chen F, Huang XZ, Yang M *et al.* 2006. Westerly dominated Holocene climate model in arid Central Asia – Case study on Bosten Lake, Xinjiang, China (in Chinese). *Quaternary Sciences* **26**: 881–887.

Chen F, Xu Q, Chen J *et al.* 2015. East Asian summer monsoon precipitation variability since the last deglaciation. *Scientific Reports* **5** 11186.

Chen JH, Rao ZG, Liu JB *et al.* 2016. On the timing of the East Asian summer monsoon maximum during the Holocene – does the speleothem oxygen isotope record reflect monsoon rainfall variability? *Science China Earth Sciences* **59**: 2328–2338.

Collins WD, Bitz CM, Blackmon ML *et al.* 2006. The community climate system model version 3 (CCSM3). *Journal of Climate* **19**: 2122–2143.

Compilatory Commission of Annals of Hexigten Banner. 1993. *Annals of Hexigten Banner*. People's Press of Inner Mongolia: Hohhot.

Dietze M, Kreutzer S, Burow C *et al.* 2016. The Abanico plot: visualising chronometric data with individual standard errors. *Quaternary Geochronology* **31**: 12–18.

Ding ZL, Derbyshire E, Yang SL *et al.* 2005. Stepwise expansion of desert environment across northern China in the past 3.5 Ma and implications for monsoon evolution. *Earth and Planetary Science Letters* **237**: 45–55.

Dykoski CA, Edwards RL, Cheng H *et al.* 2005. A high-resolution, absolute-dated Holocene and deglacial Asian monsoon record from Dongge Cave, China. *Earth and Planetary Science Letters* **233**: 71–86.

Fan J, Xiao J, Wen R *et al.* 2017. Carbon and nitrogen signatures of sedimentary organic matter from Dali Lake in Inner Mongolia: implications for Holocene hydrological and ecological variations in the East Asian summer monsoon margin. *Quaternary International* **452**: 65–78.

Fan J, Xiao J, Wen R *et al.* 2019. Mineralogy and carbonate geochemistry of the Dali Lake sediments: implications for paleohydrological changes in the East Asian summer monsoon margin during the Holocene. *Quaternary International* **527**: 103–112.

Gao Z. 1988. The changes of Dalainor Lake (in Chinese). *Geographical Research* **7**: 40–47.

Goldsmith Y, Broecker WS, Xu H *et al.* 2017. Northward extent of East Asian monsoon covaries with intensity on orbital and millennial timescales. *Proceedings of the National Academy of Sciences of the United States of America* **114**: 1817–1821.

Han F, Li X, Gao L. 2007. The dynamic characteristics of Dalinuoer wetland in Inner Mongolia based on remote sensing (in Chinese). *Journal of Inner Mongolia Agricultural University (Natural Science Edition)* **1**: 017.

He F, Shakun JD, Clark PU *et al.* 2013. Northern Hemisphere forcing of Southern Hemisphere Climate during the last deglaciation. *Nature* **494**: 81–85.

Jacobs Z, Duller GAT, Wintle AG. 2003. Optical dating of dune sand from Blombos Cave, South Africa: II – single grain data. *Journal of Human Evolution* **44**: 613–625.

Dong J, Wang Y, Cheng H *et al.* 2010. A high-resolution stalagmite record of the Holocene East Asian monsoon from Mt Shennongjia, central China. *The Holocene* **20**: 257–264.

Lambeck K, Rouby H, Purcell A *et al.* 2014. Sea level and global ice volumes from the Last Glacial Maximum to the Holocene. *Proceedings of the National Academy of Sciences of the United States of America* **111**: 15296–15303.

Laskar J, Robutel P, Joutel F *et al.* 2004. A long-term numerical solution for the insolation quantities of the Earth. *Astronomy and Astrophysics* **428**: 261–285.

Lee J, Li S, Aitchison JC. 2009. OSL dating of paleoshorelines at Lagkor Tso, western Tibet. *Quaternary Geochronology* **4**: 335–343.

Lian OB, Roberts RG. 2006. Dating the Quaternary: progress in luminescence dating of sediments. *Quaternary Science Reviews* **25**: 2449–2468.

Liu J, Chen S, Chen J *et al.* 2017. Chinese cave $\delta^{18}O$ records do not represent northern East Asian summer monsoon rainfall. *Proceedings of the National Academy of Sciences of the United States of America* **114**: E2987–E2988.

Liu J, Wang Y, Li T *et al.* 2016. Lake level fluctuation revealed by beach ridges of Dali lake in Inner Mongolia since 12.5 cal ka (in Chinese). *Journal of Palaeogeograpgy* **18**: 1044–1052.

Liu Z, Wen X, Brady EC *et al.* 2014. Chinese cave records and the East Asia summer monsoon. *Quaternary Science Reviews* **83**: 115–128.

Lu H, Miao X, Zhou Y *et al.* 2005. Late Quaternary aeolian activity in the Mu Us and Otindag dune fields (north China) and lagged response to insolation forcing. *Geophysical Research Letters* **32**: L21716.

Lu H, Yi S, Liu Z *et al.* 2013a. Variation of East Asian monsoon precipitation during the past 21 k.y. and potential $CO_2$ forcing. *Geology* **41**: 1023–1026.

Lu H, Yi S, Xu Z *et al.* 2013b. Chinese deserts and sand fields in Last Glacial Maximum and Holocene Optimum. *Chinese Science Bulletin* **58**: 2775–2783.

Lv C, Li X, Han Z *et al.* 2018. Fluvial response to precipitation variations since 36 ka in the Hunshandake Sandy Land in North China. *Geomorphology* **317**: 128–138.

Marzin C, Braconnot P, Kageyama M. 2013. Relative impacts of insolation changes, meltwater fluxes and ice sheets on African and Asian monsoons during the Holocene. *Climate Dynamics* **41**: 2267–2286.

Monnin E, Steig EJ, Siegenthaler U *et al.* 2004. Evidence for substantial accumulation rate variability in Antarctica during the Holocene, through synchronization of $CO_2$ in the Taylor Dome, Dome C and DML ice cores. *Earth and Planetary Science Letters* **224**: 45–54.

Murray AS, Wintle AG. 2000. Luminescence dating of quartz using an improved single-aliquot regenerative-dose protocol. *Radiation Measurements* **32**: 57–73.

Murray AS, Wintle AG. 2003. The single aliquot regenerative dose protocol: potential for improvements in reliability. *Radiation Measurements* **37**: 377–381.

Nott J, Smithers S, Walsh K *et al.* 2009. Sand beach ridges record 6000 year history of extreme tropical cyclone activity in northeastern Australia. *Quaternary Science Reviews* **28**: 1511–1520.

Rades EF, Tsukamoto S, Frechen M *et al.* 2015. A lake-level chronology based on feldspar luminescence dating of beach ridges at Tangra Yum Co (southern Tibet). *Quaternary Research* **83**: 469–478.

Reheis MC, Adams KD, Oviatt CG *et al.* 2014. Pluvial lakes in the Great Basin of the western United States—a view from the outcrop. *Quaternary Science Reviews* **97**: 33–57.

Shakun JD, Clark PU, He F *et al.* 2012. Global warming preceded by increasing carbon dioxide concentrations during the last deglaciation. *Nature* **484**: 49–54.

Smith GI, Street-Perrott FA. 1983. Pluvial lakes of the western United States. *Late Quaternary environments of the United States* **1**: 190–212.

Sun X, Chen L, He J. 2002. Index of land-sea thermal difference and its relation to interannual variation of summer circulation and rainfall over East Asia (in Chinese). *Acta Meteorologica Sinica* **60**: 164–172.

Tsakalos E, Christodoulakis J, Charalambous L. 2016. The dose rate calculator (DRc) for luminescence and ESR dating – a Java application for dose rate and age determination. *Archaeometry* **58**: 347–352.

Wang Y, Cheng H, Edwards RL *et al.* 2008. Millennial- and orbital-scale changes in the East Asian monsoon over the past 224,000 years. *Nature* **451**: 1090–1093.

Wen R, Xiao J, Fan J *et al.* 2017. Pollen evidence for a mid-Holocene East Asian summer monsoon maximum in northern China. *Quaternary Science Reviews* **176**: 29–35.

Xiao J, Chang Z, Si B *et al.* 2009. Partitioning of the grain-size components of Dali Lake core sediments: evidence for lake-level changes during the Holocene. *Journal of Paleolimnology* **42**: 249–260.

Xiao J, Si B, Zhai D *et al.* 2008. Hydrology of Dali lake in central-eastern Inner Mongolia and Holocene East Asian monsoon variability. *Journal of Paleolimnology* **40**: 519–528.

Xu Q, Xiao J, Li Y *et al.* 2010. Pollen-based quantitative reconstruction of Holocene climate changes in the Daihai Lake area, Inner Mongolia, China. *Journal of Climate* **23**: 2856–2868.

Yang X, Scuderi LA, Wang X *et al.* 2015. Groundwater sapping as the cause of irreversible desertification of Hunshandake Sandy Lands, Inner Mongolia, northern China. *Proceedings of the National Academy of Sciences of the United States of America* **112**: 702–706.

Zhang H, Tian M, Guo J *et al.* 2012. The dynamic monitoring of Dalinur Lake in Inner Mongolia during 1999–2010 based on RS and GIS (in Chinese). *Journal of Arid Land Resources and Environment* **10**: 008.

Zhang X, Jin L, Chen J *et al.* 2018. Lagged response of summer precipitation to insolation forcing on the northeastern Tibetan Plateau during the Holocene. *Climate Dynamics* **50**: 3117–3129.

Zhou Y, Han Z, Li X *et al.* 2018. Sandy loess records of precipitation changes and monsoon migrations in the Hunshandake Sandy Land since the Last Glacial Maximum. *Paleoceanography and Paleoclimatology* **33**: 945–957.

Zhou YL, Lu HY, Zhang XY *et al.* 2013. Changes of the border of Otindag sand field (northern China) during the Last Glacial maximum and Holocene optimum (in Chinese). *Quaternary Sciences* **33**: 228–242.